Enhanced Electrochemical Performance of $Fe_{0.74}Sn_5$@Reduced Graphene Oxide Nanocomposite Anodes for Both Li-Ion and Na-Ion Batteries

Feng-Xia Xin, Hua-Jun Tian, Xiao-Liang Wang,[†] Wei Xu, Wen-Ge Zheng, and Wei-Qiang Han*

Ningbo Institute of Materials Technology & Engineering (NIMTE), Chinese Academy of Sciences, Ningbo 315201, P. R. China

Ⓢ Supporting Information

ABSTRACT: The recently found intermetallic $FeSn_5$ phase with defect structure $Fe_{0.74}Sn_5$ has shown promise as a high capacity anode for lithium-ion batteries (LIBs). The theoretical capacity is as high as 929 mAh g^{-1} thanks to the high Sn/Fe ratio. However, despite being an alloy, the cycle life remains a great challenge. Here, by combining $Fe_{0.74}Sn_5$ nanospheres with reduced graphene oxide (RGO) nanosheets, the $Fe_{0.74}Sn_5$@RGO nanocomposite can achieve capacity retention 3 times that of the nanospheres alone, after 100 charge/discharge cycles. Moreover, the nanocomposite also displays its versatility as a high-capacity anode in sodium-ion batteries (SIBs). The enhanced cell performance in both battery systems indicates that the $Fe_{0.74}Sn_5$@RGO nanocomposite can be a potential anode candidate for the application of Li-ion and Na-ion battery.

KEYWORDS: Li-ion battery, Na-ion battery, anode, nanocomposite, electrochemical performance
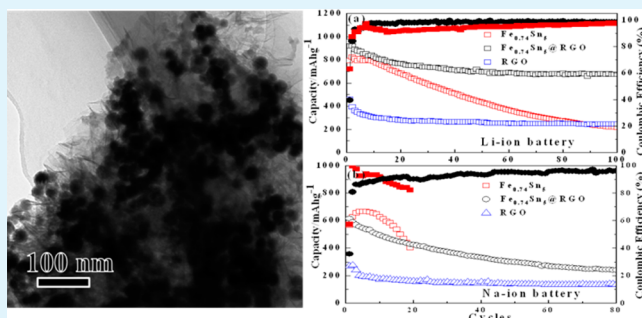
■ INTRODUCTION

Rechargeable lithium-ion batteries (LIBs) are currently the most popular power source for electric vehicles.[1−5] Meanwhile, conceptually identical sodium-ion batteries (SIBs) also received much interest as an alternative due to the low cost and environmental benefits.[6−9] In both battery systems, high-capacity anode materials hold the key to meeting future high energy density requirements. Therefore, tin (Sn)-based systems have been studied extensively.[10,11] As an anode material in LIBs, Sn has high theoretical gravimetric capacity (994 mAh g^{-1}) and volumetric capacity (7313 mAh cm^{-3}), as compared with 372 mAh g^{-1} and 883 mAh cm^{-3} of the state-of-the-art graphite. Meanwhile, Sn can electrochemically alloy with Na and form a $Na_{15}Sn_4$ alloy, delivering a theoretical capacity of 847 mAh g^{-1}.[12,13] The fact that a sodium ion cannot intercalate into graphite makes Sn very appealing in SIBs.

The major challenge for Sn anodes in both battery systems is the poor cycling stability due to the large volume change (257% in LIB and 420% in SIB, respectively) upon charge/discharge processes.[14−16] Therefore, many efforts have been made to improve the electrochemical performance, such as Sn-based oxide,[17] Sn−M (M = active/inactive metal) alloys, Sn−C materials,[18] and their composites.[19−25] The main idea behind these approaches is to buffer the volume change, via incorporating alien species to Sn.

Recently, we reported a new intermetallic $FeSn_5$ phase, which appeared to supplement the existing Fe−Sn intermetallics (FeSn, $FeSn_2$, and Fe_5Sn_3) in the phase diagram.[26] It is thought that the defect structure of $Fe_{0.74}Sn_5$ can stabilize the phase at room temperature. Its theoretical capacity of 929 mAh g^{-1} was the highest among the reported M (electrochemically inactive)−Sn intermetallic anodes in LIBs. As expected, the $Fe_{0.74}Sn_5$ nanospheres showed much higher capacity than the intensively studied $FeSn_2$ and could stabilize capacity for 15 cycles. However, afterward, the capacity started to fade rapidly. Presumably, the material could experience fatigue failure after 15 cycles, and a new mechanism is needed to further improve its cycling stability.

To address the issue on cycling stability, reduced graphene oxide became of great interest to us. It can act as a superior substrate to load electrochemically active materials and relieve the large volume changes, resulting in improved cycle life.[24,27] In another prior work, we blended graphene nanosheets with porous Si nanowires in the anode film.[28] The capacity of Si nanowires was doubled as compared with their capacity in the presence of regular carbon black. The anode also maintained good cycling stability.

Herein, we made a $Fe_{0.74}Sn_5$@RGO nanocomposite for the first time through a one-pot wet chemistry synthesis and demonstrate the combining effect of $Fe_{0.74}Sn_5$ and RGO on extending the anode's cycle life with high capacity. Moreover, it

is interesting that the improvement can be applied to both LIBs and SIBs.

■ EXPERIMENTAL SECTION

Synthesis of the $Fe_{0.74}Sn_5$@RGO Nanocomposite. The RGO sheets used were prepared by a modified Hummers method[29] and then were reduced as previously reported.[30] The $Fe_{0.74}Sn_5$@RGO composite was synthesized as follows (Scheme 1). First, 25 mg of

Scheme 1. Schematic Diagram of the Preparation Process for a $Fe_{0.74}Sn_5$@RGO Nanocomposite
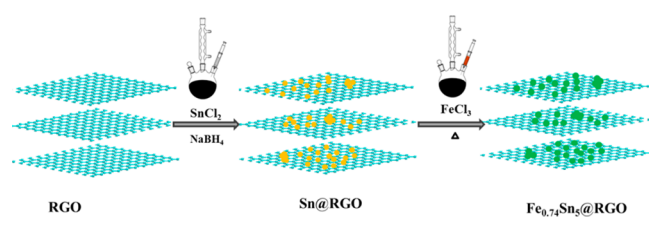
RGO was dispersed in 35 mL of tetraethylene glycol (TEG, 99%) by sonication for 1 h and transferred into a three-necked flask in a Schlenk line. Amounts of 1.57 g of polyvinylpyrrolidone (PVP, MW = 360 000) and 0.66 g of poly(2-ethyl-2-oxazoline) (PEtOx, MW = 50 000) were dissolved with vigorous stirring. Then the solution was heated to 170 °C, and a tin(II) chloride (SnCl$_2$, anhydrous, 99%) solution (0.3 g in 4 mL of TEG) was mixed. After 10 min, 0.6 g of sodium borohydride (NaBH$_4$, 98%) in 20 mL of TEG as a reducing agent was introduced drop by drop. After about 30 min, the temperature of the suspensions was increased to 205 °C under argon; an iron(III) chloride (FeCl$_3$ anhydrous reagent grade, 97%) solution (0.01930 g of FeCl$_3$ in 4 mL of TEG) was injected into the mixture. The suspension was stirred 1 h before it was cooled to room temperature. The $Fe_{0.74}Sn_5$@RGO composite was harvested by centrifugation and washed with ethanol several times. For comparison, $Fe_{0.74}Sn_5$ nanocrystals were also prepared in the same conditions but without the presence of RGO.

Materials Characterization. The collected products were characterized by X-ray diffractometry (XRD) on a D8 Diffractometer from Bruker instruments (Cu Kα radiation = 0.154 nm) equipped with a scintillation counter at a scanning rate of 0.02°/s. The morphology of the samples was observed by scanning electron microscopy (SEM, Hitachi, S-4800) using an operating voltage of 8 kV with an energy-dispersive X-ray spectroscopy (EDS) detector and transmission electron microscopy (TEM, Tecnai F20). Raman spectra were recorded on a Renishaw in Via Reflex Raman system by exciting a 532 nm Ar$^+$ laser. The weight ratio between $Fe_{0.74}Sn_5$ and graphene was determined by thermogravimetric analysis using a Pysis Diamond simultaneous TG/DTA analyzer between 50 and 900 °C at a heating rate of 5 °C/min in air.

Electrochemical Performance Testing. The electrochemical properties of the materials were evaluated using CR2032-type coin cells, which were assembled in an argon-filled glovebox with both moisture and oxygen contents below 0.1 ppm. The working electrode films were composed of the 80 wt % active material ($Fe_{0.74}Sn_5$@RGO composite), 10 wt % carbon black (Super P), and 10 wt % poly(acrylic acid) binder. For assembling Li-ion batteries, a lithium foil served as both the counter and reference electrodes. The Celgard 2300 membrane was used as the separator, and 1 M solution of LiPF$_6$ in ethylene carbonate/dimethyl carbonate (EC/DMC, 1:1 in volume) was used as the electrolyte solution. For assembling Na-ion batteries, a Na foil, glass fiber, and 1 M solution of NaPF$_6$ in ethylene carbonate/dimethyl carbonate (EC/DMC, 1:1 in volume) was utilized as the counter electrode, the separator, and the electrolyte, respectively. All galvanostatic charging/discharging and GITT tests were conducted on an Arbin MSTAT system with the voltage range of 0.005−2.0 V at room temperature. Cyclic voltammetry (CV) between 0.005 and 2 V at a scan rate of 0.02 mV/s was recorded using a Solatron 1470E

Electrochemical Interface in Li-ion and Na-ion batteries. The EIS of the $Fe_{0.74}Sn_5$@RGO nanocomposite anode was tested with the frequency ranging from 1 MHz to 0.001 Hz and an AC signal of 10 mV in amplitude as the perturbation.

■ RESULTS AND DISCUSSION

The crystallographic phases of bare RGO, $Fe_{0.74}Sn_5$ nanospheres, and the $Fe_{0.74}Sn_5$@RGO nanocomposite were identified by XRD (Figure 1). Strong diffraction peaks are
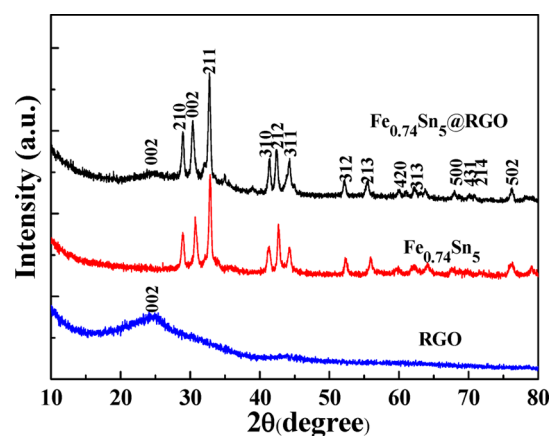
**Figure 1.** XRD patterns of bare RGO, bare $Fe_{0.74}Sn_5$, and the $Fe_{0.74}Sn_5$@RGO nanocomposite.

observed in $Fe_{0.74}Sn_5$ and $Fe_{0.74}Sn_5$@RGO nanocomposite samples. The pattern can be indexed to the tetragonal structure FeSn$_5$ in the *P4/mcc* space group.[26] A broad peak ascribed to the RGO (002) crystal plane appears at ∼25° in the $Fe_{0.74}Sn_5$@RGO nanocomposite. This result indicates that aggregation of RGO sheets persisted to some extent in RGO due to strong van der Waals interactions.[30] The XRD confirms the coexistence of RGO nanosheets and $Fe_{0.74}Sn_5$ nanospheres in the composite.

To determine the weight percentage of $Fe_{0.74}Sn_5$ nanospheres in the composite, thermogravimetry analysis (TGA) (Figure S1 in Supporting Information) was carried out on the composite sample and the $Fe_{0.74}Sn_5$ sample. The content of $Fe_{0.74}Sn_5$ nanospheres in the composite can be calculated based on the equation below

$$Fe_{0.74}Sn_5 \ (wt\%) = 100\% \times (wt \% \text{ of composite sample at } 900°C)/(wt \% \text{ of } Fe_{0.74}Sn_5 \text{ nanosphere sample at } 900°C)$$

It is determined that there is about 30 wt % RGO and 70 wt % $Fe_{0.74}Sn_5$ nanospheres in the composite.

The morphology of the $Fe_{0.74}Sn_5$@RGO nanocomposite was characterized by TEM in Figure 2a. $Fe_{0.74}Sn_5$ nanospheres are dispersed on RGO nanosheets, with the size of 30−50 nm. The small size of primary particles can avoid the widespread problem of pulverization of high capacity anode materials. In our previous work, regarding the size effort of Sn nanospheres on cell performance, we found out that nanospheres with 45 nm had better stability and higher capacity.[31] Therefore, 30−50 nm $Fe_{0.74}Sn_5$ nanospheres in the composite were investigated here. Some agglomeration of $Fe_{0.74}Sn_5$ nanospheres existed in the nanocomposite. The HRTEM image (Figure 2b) of a $Fe_{0.74}Sn_5$ nanosphere shows a typical core−shell structure where a single-crystalline intermetallic core is covered by a 3−4
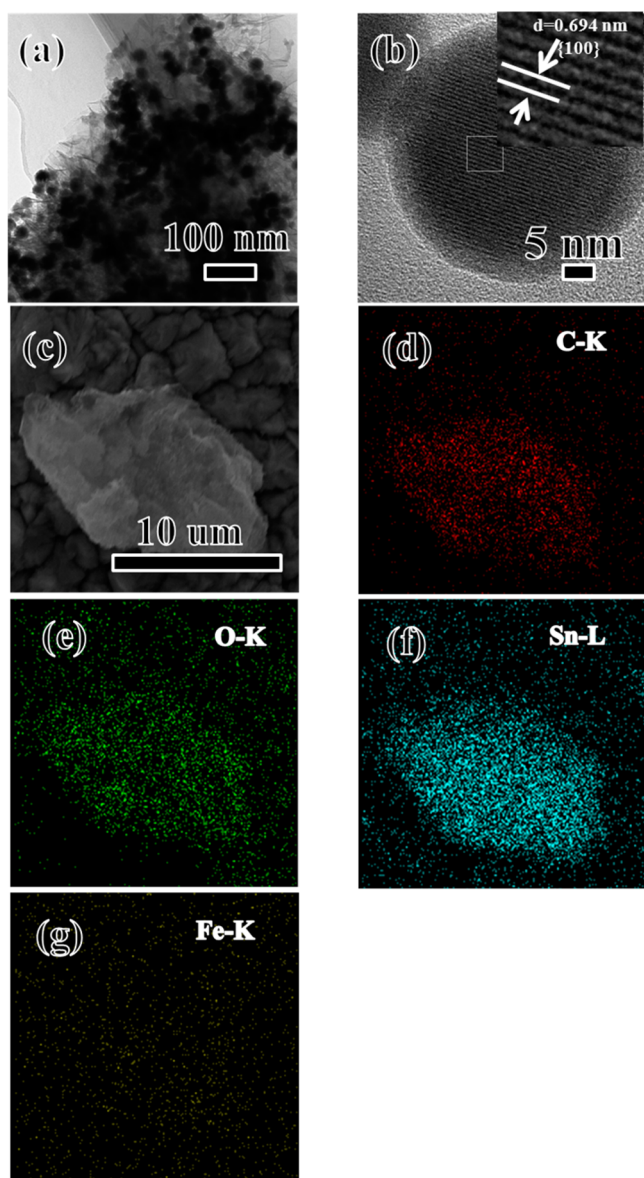
Figure 2. (a) TEM image of the $Fe_{0.74}Sn_5$@RGO nanocomposite. (b) Typical HRTEM images of the single tetragonal structure $Fe_{0.74}Sn_5$ nanosphere. (c) SEM image of $Fe_{0.74}Sn_5$@RGO nanocomposite. (d), (e), (f), and (g) EDX elemental mapping of the area of (c) for carbon, oxygen, tin, and iron, respectively.

nm thick amorphous oxide shell. The d-spacing value is 6.94 Å, corresponding to the (100) plane of $Fe_{0.74}Sn_5$ nanospheres (d(100) = 6.91 Å). The uniform distribution of the nanospheres is further evident in the EDS mapping on carbon, oxygen, tin, and iron elements (Figure 2c, 2d, 2e, 2f, and 2g) as well as the SEM images (Figure S2, Supporting Information). According to TG measurement, the weight percentage of Fe in the nanocomposite was only 4.6%. Therefore, the signal from the Fe element was much weaker.

To further understand the structural properties, Raman spectra of bare RGO, bare $Fe_{0.74}Sn_5$, and the $Fe_{0.74}Sn_5$@RGO nanocomposite were measured (Figure S3, Supporting Information). Two characteristic peaks at 1350 and 1580 cm^{-1} can be seen from the disordered (D) and graphitic (G) bands of carbon, respectively. The change in the intensity ratio of D and G bands (I_D:I_G) from 0.843 in RGO to 0.885 in

$Fe_{0.74}Sn_5$@RGO may be due to the insertion of $Fe_{0.74}Sn_5$ nanospheres between RGO sheets, resulting in a more disordered structure and more defects than pristine RGO.[32] The broad peaks at 2695 cm^{-1} (2D) and 2910 cm^{-1} (D+G) suggest the few-layer nature of the RGO.
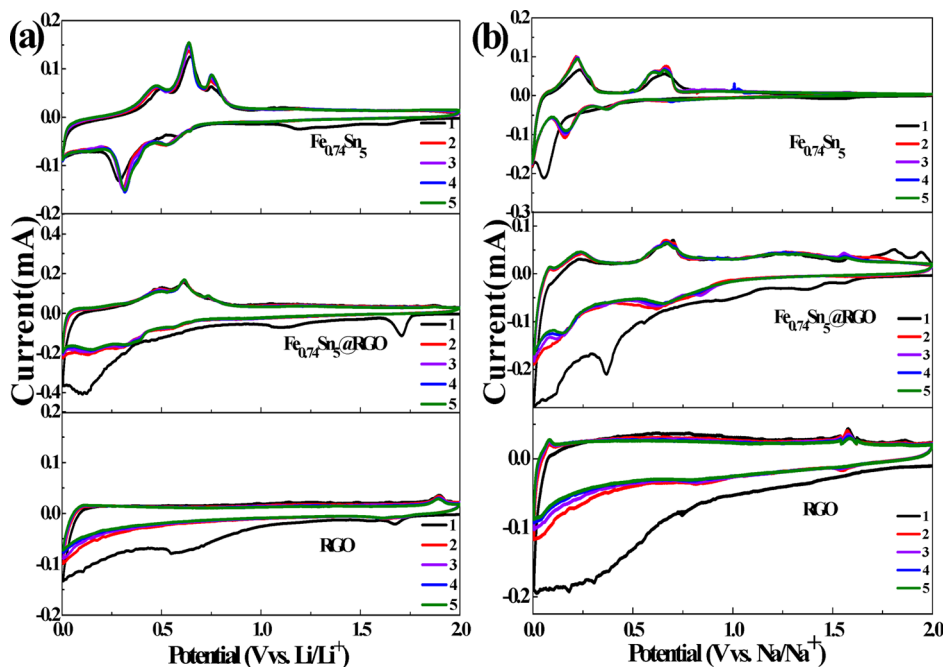
The $Fe_{0.74}Sn_5$@RGO nanocomposite exhibits enhanced capacity and cycling stability, in both LIBs and SIBs. Theoretically, $Fe_{0.74}Sn_5$ itself has high capacities of 929 and 792 mAh g^{-1} as the anode in Li-ion and Na-ion batteries, respectively. The existence of Fe vacancies makes the theoretical capacity of $Fe_{0.74}Sn_5$ higher than that of stoichiometric $FeSn_5$, i.e., 929 versus 908 mAh g^{-1} as Li-ion anode and 792 versus 774 mAh g^{-1} as Na-ion anode. It is noted that Fe does not form alloy with either Li or Na.[11,33] Thus, to our best knowledge, $Fe_{0.74}Sn_5$ has the highest capacity among the reported M (electrochemically inactive)−Sn intermetallic anodes for SIBs.

As shown in Figure 3, $Fe_{0.74}Sn_5$ nanospheres alone could deliver 820 and 670 mAh g^{-1} in Li-ion and Na-ion batteries. However, the capacity starts to drop fast after 15 cycles in the case of LIBs and after 8 cycles in the case of SIBs. Diffraction peaks (Figure S4a, Supporting Information) which are indexed to the cubic structure Sn appear for the $Fe_{0.74}Sn_5$ anode in the Li-ion battery after much cycling due to the agglomeration of Sn particles. On the other hand, the existence of cubic and tetragonal structure Sn (Figure S4b, Supporting Information) is identified in the Na-ion battery. On the contrary, the RGO anode has long cycling stability but low capacity, which may be due to irreversible aggregation and/or stacking upon charge/discharge cycles.[34] The $Fe_{0.74}Sn_5$@RGO nanocomposite shows much better cycling stability than $Fe_{0.74}Sn_5$ as well as higher capacity than that of RGO. After 100 and 80 discharge/charge cycles, the $Fe_{0.74}Sn_5$ in the composite anode can retain 674 and 240 mAh g^{-1} for Li-ion and Na-ion batteries, respectively. The enhanced cycling stability can be related to the following characteristics: (1) The flexible and conductive RGO sheets can adhere to $Fe_{0.74}Sn_5$ nanospheres to keep electrical contact and offer a "buffer zone". Thus, they effectively accommodate the mechanical strain from large volume change during lithium/sodium insertion/extraction.[35] (2) The presence of $Fe_{0.74}Sn_5$ nanospheres in the composite can relieve irreversible aggregation and/or stacking of individual RGO nanosheets.[34] Meanwhile, RGO can circumvent the aggregation of $Fe_{0.74}Sn_5$ nanospheres.[36] (3) Large void volume between the nanoparticles and RGO sheets can promote easy penetration of the electrolyte.[37] (4) RGO contributes to the capacity due to Li/Na storage on both sides of graphene and/or at edges, vacancies, and disorder/covalent sites.[38] In addition, the $Fe_{0.74}Sn_5$@RGO nanocomposite anode also exhibits moderate rate capability between 50−1000 mA g^{-1} in Li-ion battery (Figure 3c) and 20−500 mA g^{-1} in the Na-ion battery (Figure 3d).

To understand the electrochemical behavior of the $Fe_{0.74}Sn_5$@RGO electrode, Figure 4 shows the cyclic voltammetry (CV) curves of $Fe_{0.74}Sn_5$ nanospheres, $Fe_{0.74}Sn_5$@RGO, and bare RGO anodes. No obvious current peaks are present in the bare RGO anode.[36,39] During the first lithiation of $Fe_{0.74}Sn_5$, a broad peak at 1.2−1.7 V is observed but is absent in the second cycle. This peak can be attributed the formation of solid−electrolyte interface (SEI) films and/or the irreversible lithiation of the surface oxidized layer. The reduction peaks around 0.35 V (0.01 V) and 0.6 V (0.15 V) are due to lithium/sodium insertion. The peaks in the positive current include every dealloying step. For $Fe_{0.74}Sn_5$@RGO
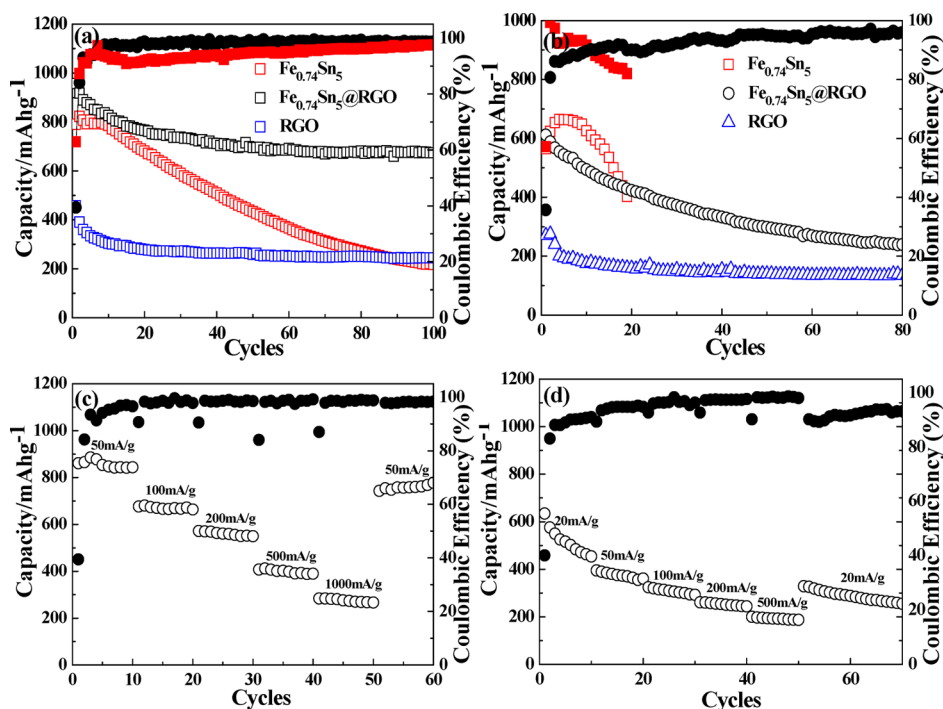
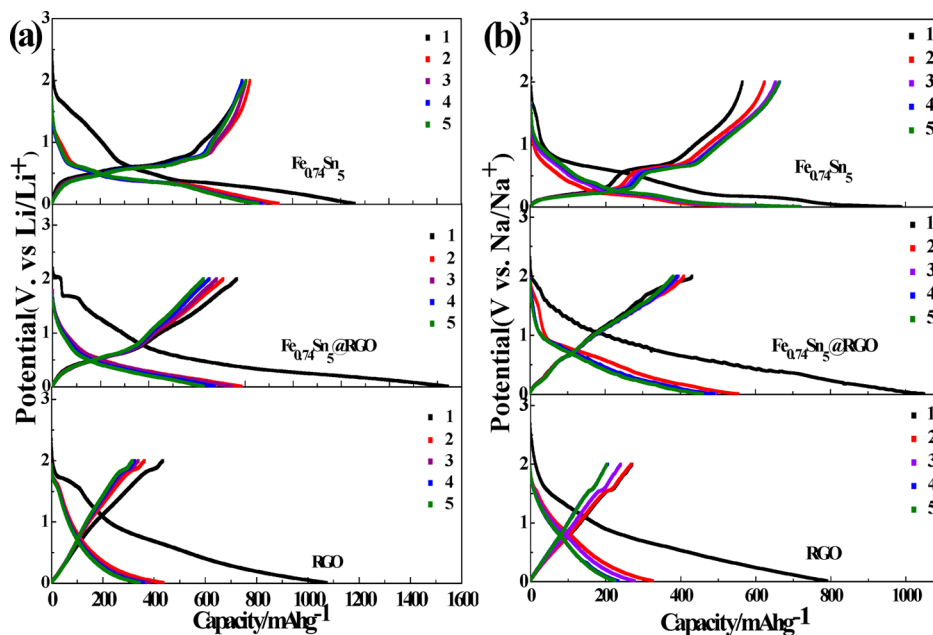**Figure 3.** (a, b) Cycling performance of $Fe_{0.74}Sn_5$ nanospheres, the $Fe_{0.74}Sn_5$@RGO nanocomposite, and bare graphene at 50 mA/g current density in Li-ion battery and 20 mA/g current density for Na-ion battery. The Coulombic efficiencies of $Fe_{0.74}Sn_5$ nanospheres and $Fe_{0.74}Sn_5$@RGO nanocomposite are denoted by a solid square (red) and solid circle (black). (c, d) Rate performance of the $Fe_{0.74}Sn_5$@RGO nanocomposite at varied current densities in Li-ion battery and Na-ion battery (note that the capacity values in the $Fe_{0.74}Sn_5$@RGO nanocomposite in the graph were calculated based on $Fe_{0.74}Sn_5$ particles).


Figure 4. (a, b) Cyclic voltammograms of bare RGO, $Fe_{0.74}Sn_5$ nanospheres, and the $Fe_{0.74}Sn_5$@RGO nanocomposite of the initial five cycles scanned at a rate of 0.02 mV/s between 0.005 and 2 V in Li-ion and Na-ion batteries.

anode materials, during the first discharge, similarly, the broad cathodic peaks above 1.0 V mainly come from the SEI formation.[40] The reduction peaks between 0.1 and 0.7 V correspond to the formation of Li_xSn alloys (Figure 4a).[11] Three broad anodic peaks located at around 0.49, 0.61, and 0.73 V result from the delithiation processes of the Li_xSn alloys,

which are absent in RGO. On the other hand, the desodiation of the $Fe_{0.74}Sn_5$@RGO anode at the same scan rate (Figure 4b) shows two distinct anodic peaks at around 0.25 and 0.7 V.[12] In both cases, the almost identical curves from the second cycle to the fifth cycle suggest good reversibility of the $Fe_{0.74}Sn_5$@RGO composite.

Figure 5. (a, b) Galvanostatic charge and discharge curves of $Fe_{0.74}Sn_5$ nanospheres, the $Fe_{0.74}Sn_5$@RGO nanocomposite, and bare RGO anodes of the initial five cycles between 0.005 and 2 V at 50 mA/g current density for Li-ion battery and 20 mA/g for Na-ion battery.
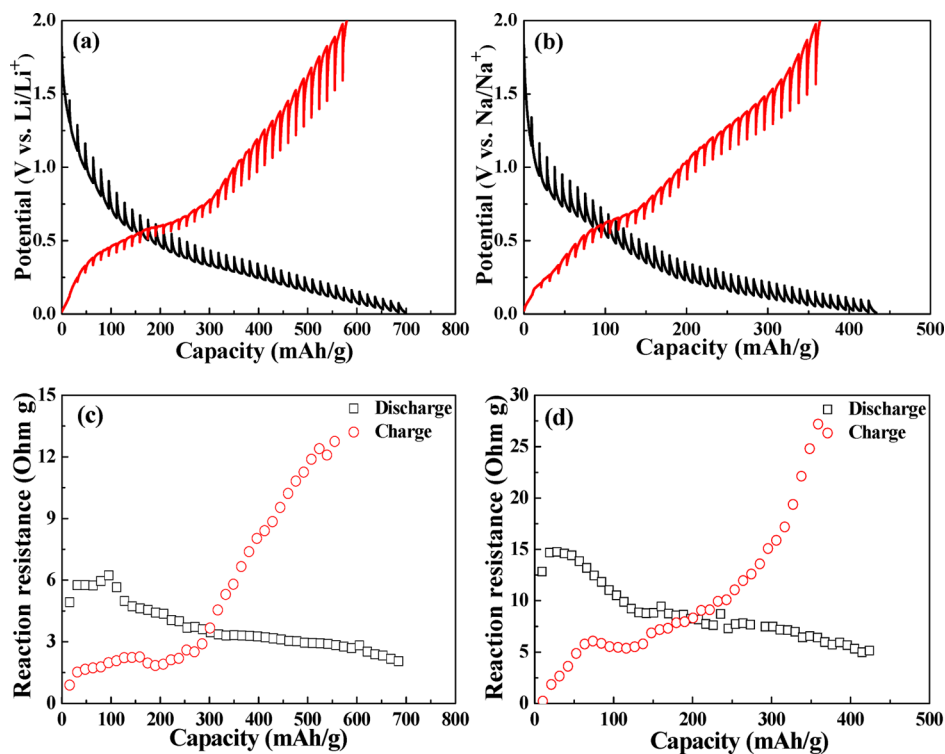
Figure 6. (a, b) Potential response and (c, d) reaction resistance of the $Fe_{0.74}Sn_5$@RGO nanocomposite during GITT measurement (a, c) in a Li-ion cell at 20 mA/g and (b, d) in a Na-ion cell at 10 mA/g for the second cycle.

Figure 5 documents galvanostatic charge and discharge curves of the $Fe_{0.74}Sn_5$@RGO nanocomposite anode for the initial five cycles at a current density of 50 mA g^{-1} for Li-ion battery and 20 mA g^{-1} for Na-ion battery. For comparison, the results of $Fe_{0.74}Sn_5$ nanospheres and pure RGO are also presented. During the first lithiation/delithiation, the specific discharge and charge capacities are 1256 and 790 mAh g^{-1} for $Fe_{0.74}Sn_5$ nanospheres, 1073 and 435 mAh g^{-1} for bare RGO nanosheets, and 1554 and 671 mAh g^{-1} for the $Fe_{0.74}Sn_5$@

RGO nanocomposite. For the nanocomposite, lithiation mainly occurs below 0.5 V, which is similar to $Fe_{0.74}Sn_5$ nanospheres. However, its plateaus are not as pronounced as the ones in $Fe_{0.74}Sn_5$ nanospheres. During charging, the nanocomposite exhibits a change in slope at around 300 mAh g^{-1}. The profile of the nanocomposite suggests that the (de)lithiation processes are controlled by both $Fe_{0.74}Sn_5$ and RGO.

For the SIB application, in Figure 5b, the major Na–Sn alloying voltages are around 0.2 and 0.01 V for $Fe_{0.74}Sn_5$

nanospheres. The desodiation curve consists of two plateaus: one between 0.1 and 0.3 V and the other around 0.6 V. These potential plateaus are in good agreement with the CV peaks. Again, the (de)sodiation plateaus are not as obvious in the composite as in the $Fe_{0.74}Sn_5$ nanospheres, reflecting the influence from RGO. In addition, the lower capacity in Na-ion batteries than in Li-ion batteries may be related to the poor electrochemical alloying/dealloying kinetics since Na ions are about 55% larger than Li ions in radius.[12]

Figure 6 represents the potential response during the galvanostatic intermittent titration technique (GITT) measurement. The equal duration of pulses is 0.5 h, while the rest time is set for 4 h to reach quasi-equilibrium potentials. It is clear that the discharge overpotential of both battery systems decreases with the state of discharge (SoD), which means that the diffusion length was becoming shorter.[41] The volume contraction during lithium/sodium extraction worsens the contact between particles, leading to the increase of the charging overpotential as the state of charge (SoC) increases. The overpotential during the pulse is proportional to the reaction resistance. Low reaction resistance can result from low electrolyte resistance, good kinetics of the surface charge transfer, or fast ionic diffusion. In both battery systems, the reaction resistance decreases during discharging and exhibits a gradual increase during charging. The average resistance of the $Fe_{0.74}Sn_5$@RGO nanocomposite anode in the Na-ion battery is about two times higher than that in the Li-ion battery. The findings are also confirmed by the GITT results during the first cycle (Figure S5, Supporting Information). Further, the diffusion coefficient of Li ions and Na ions in the $Fe_{0.74}Sn_5$@RGO nanocomposite anode for both Li-ion and Na-ion batteries has been extracted from GITT for the second cycle (Figure S6, Supporting Information). The lithium-ion diffusion coefficient in the $Fe_{0.74}Sn_5$@RGO anode was on the order of $10^{-10} \sim 10^{-12}$ cm^2/s, and the diffusion coefficient of the sodium ion was $10^{-11} \sim 10^{-13}$ cm^2/s. The higher Li-ion diffusion coefficient than the one in Na-ion batteries could be attributed to the smaller size of Li ions in radius.

In addition, electrochemical impedance spectroscopy (EIS) was taken after the cells were discharged to 0.3 V, as shown in Figure 7. The plot consists of one arc in the high frequency region which can be associated with SEI and charge-transfer processes and a slanted line in the low-frequency region due to the Li$^+$/Na$^+$ ion diffusion. As seen, the larger semicircle in the
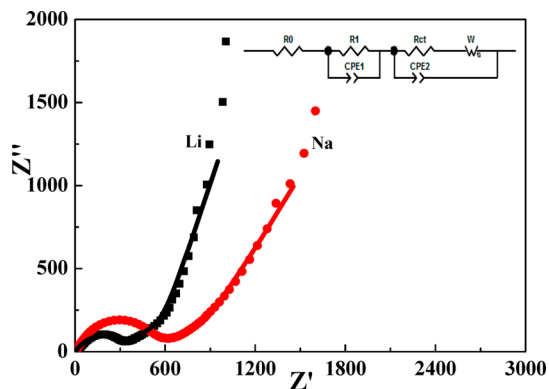
Na-ion battery implies a thicker SEI layer and/or poorer kinetics of the surface charge transfer than the Li-ion battery. Slower diffusion of Na$^+$ ions than that of Li$^+$ ions can be reflected by the long low-frequency tail. Further, the electrochemical system of $Fe_{0.74}Sn_5$@RGO in Li-ion and Na-ion batteries can be modeled and interpreted with the help of the equivalent circuit shown in the inset of Figure 7,[42] where R_0 is the electrolyte resistance, R_1 the resistance between the SEI film and the electrolyte, R_{ct} the charge-transfer resistance between the SEI and $Fe_{0.74}Sn_5$@RGO nanocomposites, and CPE1 and CPE2 are the capacitance of the SEI and the double layer on $Fe_{0.74}Sn_5$@RGO nanocomposite. The interface resistance decreased from 520 to 310 Ω in Nyquist plots for the $Fe_{0.74}Sn_5$@RGO nanocomposites in Na-ion and Li-ion batteries displaying a depressed semicircle in the high-middle-frequency region and an oblique straight line in the low-frequency region. The EIS results are in good agreement with the total reaction resistance measured using GITT.

CONCLUSION

A $Fe_{0.74}Sn_5$@RGO nanocomposite was successfully synthesized via a simple modified wet-chemistry process. It presents as a high-performance anode material for both Li-ion and Na-ion batteries. The $Fe_{0.74}Sn_5$ nanospheres obtained are 30−50 nm in size and dispersed on RGO sheets. $Fe_{0.74}Sn_5$ nanospheres in the composite can deliver capacities of 957 and 611 mAh g^{-1} for LIBs and SIBs, respectively. $Fe_{0.74}Sn_5$ in the composite can retain 674 mAh g^{-1} in LIBs and 240 mAh g^{-1} in SIBs after 100 and 80 discharge/charge cycles, respectively. The enhanced electrochemical performance indicates that the designed structure of nanosized $Fe_{0.74}Sn_5$ dispersed on conducting RGO sheets accommodates structural strain, improves electrical conductivity, and shortens transportation lengths for both Li/Na ions and electrons. Furthermore, GITT and EIS measurements reveal high resistance, slow diffusion of ions, poor kinetics of charge transfer and thick SEI layer when used for SIBs, which would explain the difference in the degree of improvement in two battery systems.

ASSOCIATED CONTENT

S Supporting Information

Additional curves and figures including TG, SEM, Raman spectra, XRD, and GITT. This material is available free of charge via the Internet at http://pubs.acs.org.

AUTHOR INFORMATION

Corresponding Author

*E-mail: hanweiqiang@nimte.ac.cn.

Present Address

†Seeo Inc., 3906 Trust Way, Hayward, CA 94545.

Notes

The authors declare no competing financial interest.

ACKNOWLEDGMENTS

Figure 7. Electrochemical impedance spectroscopy of $Fe_{0.74}Sn_5$@RGO nanocomposite anodes after two charge/discharge cycles for Li-ion and Na-ion cells in a Nyquist plot. The lines show the fitted results in Nyquist plots. (The inset shows the equivalent circuit.)

■ REFERENCES

(1) Dunn, B.; Kamath, H.; Tarascon, J. M. Electrical Energy Storage for the Grid: A Battery of Choices. *Science* **2011**, *334*, 928−935.

(2) Armand, M.; Tarascon, J. M. Building Better Batteries. *Nature* **2008**, *451*, 652−657.

(3) Li, H.; Wang, Z.; Chen, L.; Huang, X. Research on Advanced Materials for Li-Ion Batteries. *Adv. Mater.* **2009**, *21*, 4593−4607.

(4) Reddy, M. V.; Subba Rao, G. V.; Chowdari, B. V. Metal Oxides and Oxysalts as Anode Materials for Li Ion Batteries. *Chem. Rev.* **2013**, *113*, 5364−5457.

(5) Zhu, Z.; Wang, S.; Du, J.; Jin, Q.; Zhang, T.; Cheng, F.; Chen, J. Ultrasmall Sn Nanoparticles Embedded in Nitrogen-Doped Porous Carbon as High-Performance Anode for Lithium-Ion Batteries. *Nano Lett.* **2014**, *14*, 153−157.

(6) Yuan, S.; Huang, X. L.; Ma, D. L.; Wang, H. G.; Meng, F. Z.; Zhang, X. B. Engraving Copper Foil to Give Large-Scale Binder-Free Porous CuO Arrays for a High-Performance Sodium-Ion Battery Anode. *Adv. Mater.* **2014**, *26*, 2273−2279.

(7) Wu, L.; Hu, X.; Qian, J.; Pei, F.; Wu, F.; Mao, R.; Ai, X.; Yang, H.; Cao, Y. Sb-C Nanofibers with Long Cycle Life as an Anode Material for High-Performance Sodium-Ion Batteries. *Energy Environ. Sci.* **2014**, *7*, 323−328.

(8) Wang, Y.-X.; Lim, Y.-G.; Park, M.-S.; Chou, S.-L.; Kim, J. H.; Liu, H.-K.; Dou, S.-X.; Kim, Y.-J. Ultrafine SnO$_2$ Nanoparticle Loading onto Reduced Graphene Oxide as Anodes for Sodium-Ion Batteries with Superior Rate and Cycling Performances. *J. Mater. Chem. A* **2014**, *2*, 529−534.

(9) Slater, M. D.; Kim, D.; Lee, E.; Johnson, C. S. Sodium-Ion Batteries. *Adv. Funct. Mater.* **2013**, *23*, 947−958.

(10) Armstrong, M. J.; O'Dwyer, C.; Macklin, W. J.; Holmes, J. D. Evaluating the Performance of Nanostructured Materials as Lithium-Ion Battery Eectrodes. *Nano Res.* **2014**, *7*, 1−62.

(11) Park, C. M.; Kim, J. H.; Kim, H.; Sohn, H. J. Li-Alloy Based Anode Materials for Li Secondary Batteries. *Chem. Soc. Rev.* **2010**, *39*, 3115−3141.

(12) Xu, Y.; Zhu, Y.; Liu, Y.; Wang, C. Electrochemical Performance of Porous Carbon/Tin Composite Anodes for Sodium-Ion and Lithium-Ion Batteries. *Adv. Energy Mater.* **2013**, *3*, 128−133.

(13) Qian, J.; Xiong, Y.; Cao, Y.; Ai, X.; Yang, H. Synergistic Na-Storage Reactions in Sn$_4$P$_3$ as a High-Capacity, Cycle-Stable Anode of Na-Ion Batteries. *Nano Lett.* **2014**, *14*, 1865−1869.

(14) Wang, J. W.; Liu, X. H.; Mao, S. X.; Huang, J. Y. Microstructural Evolution of Tin Nanoparticles During in Situ Sodium Insertion and Extraction. *Nano Lett.* **2012**, *12*, 5897−5902.

(15) Huang, J. Y.; Zhong, L.; Wang, C. M.; Sullivan, J. P.; Xu, W.; Zhang, L. Q.; Mao, S. X.; Hudak, N. S.; Liu, X. H.; Subramanian, A.; Fan, H.; Qi, L.; Kushima, A.; Li, J. In Situ Observation of the Electrochemical Lithiation of a Single SnO$_2$ Nanowire Electrode. *Science* **2010**, *330*, 1515−1520.

(16) Li, W.; Chou, S. L.; Wang, J. Z.; Kim, J. H.; Liu, H. K.; Dou, S. X. Sn$_{4+x}$P$_3$@Amorphous Sn-P Composites as Anodes for Sodium-Ion Batteries with Low Cost, High Capacity, Long Life, and Superior Rate Capability. *Adv. Mater.* **2014**, *26*, 4037−4042.

(17) Kim, C.; Noh, M.; Choi, M.; Cho, J.; Park, B. Critical Size of a Nano SnO$_2$ Electrode for Li-Secondary Battery. *Chem. Mater.* **2005**, *17*, 3297−3301.

(18) Yu, Y.; Gu, L.; Wang, C.; Dhanabalan, A.; van Aken, P. A.; Maier, J. Encapsulation of Sn@Carbon Nanoparticles in Bamboo-Like Hollow Carbon Nanofibers as an Anode Material in Lithium-Based Batteries. *Angew. Chem., Int. Ed.* **2009**, *48*, 6485−6489.

(19) Su, D.; Xie, X.; Wang, G. Hierarchical Mesoporous SnO Microspheres as High Capacity Anode Materials for Sodium-Ion Batteries. *Chem.—Eur. J.* **2014**, *20*, 3192−3197.

(20) Su, D.; Ahn, H.-J.; Wang, G. SnO$_2$@Graphene Nanocomposites as Anode Materials for Na-Ion Batteries with Superior Electrochemical Performance. *Chem. Commun.* **2013**, *49*, 3131−3133.

(21) Wang, Y.; Su, D.; Wang, C.; Wang, G. SnO$_2$@MWCNT Nanocomposite as a High Capacity Anode Material for Sodium-Ion Batteries. *Electrochem. Commun.* **2013**, *29*, 8−11.

(22) Wang, Y.; Wu, M.; Jiao, Z.; Lee, J. Y. Sn@CNT and Sn@C@CNT Nanostructures for Superior Reversible Lithium Ion Storage. *Chem. Mater.* **2009**, *21*, 3210−3215.

(23) Luo, B.; Wang, B.; Li, X.; Jia, Y.; Liang, M.; Zhi, L. Graphene-Confined Sn Nanosheets with Enhanced Lithium Storage Capability. *Adv. Mater.* **2012**, *24*, 3538−3543.

(24) Qin, J.; He, C. N.; Zhao, N. Q.; Wang, Z. Y.; Shi, C. S.; Liu, E. Z.; Li, J. J. Graphene Networks Anchored with Sn@Graphene as Lithium Ion Battery Anode. *ACS Nano* **2014**, *8*, 1728−1738.

(25) Liu, Y.; Xu, Y.; Zhu, Y.; Culver, J. N.; Lundgren, C. A.; Xu, K.; Wang, C. Tin-Coated Viral Nanoforests as Sodium-Ion Battery Anodes. *ACS Nano* **2013**, *7*, 3627−3634.

(26) Wang, X.-L.; Feygenson, M.; Chen, H.; Lin, C.-H.; Ku, W.; Bai, J.; Aronson, M. C.; Tyson, T. A.; Han, W.-Q. Nanospheres of a New Intermetallic FeSn$_5$ Phase: Synthesis, Magnetic Properties and Anode Performance in Li-Ion Batteries. *J. Am. Chem. Soc.* **2011**, *133*, 11213−11219.

(27) Li, N.; Song, H. W.; Cui, H.; Wang, C. X. Sn@Graphene Grown on Vertically Aligned Graphene for High-Capacity, High-Rate, and Long-Life Lithium Storage. *Nano Energy* **2014**, *3*, 102−112.

(28) Wang, X.-L.; Han, W.-Q. Graphene Enhances Li Storage Capacity of Porous Single-Crystalline Silicon Nanowires. *ACS Appl. Mater. Interfaces* **2010**, *2*, 3709−3713.

(29) Hummers, W. S., Jr; Offeman, R. E. Preparation of Graphitic Oxide. *J. Am. Chem. Soc.* **1958**, *80*, 1339−1339.

(30) Shen, B.; Lu, D. D.; Zhai, W. T.; Zheng, W. G. Synthesis of Graphene by Low-Temperature Exfoliation and Reduction of Graphite Oxide under Ambient Atmosphere. *J. Mater. Chem. C* **2013**, *1*, 50−53.

(31) Wang, X.-L.; Feygenson, M. F.; Aronson, M. C.; Han, W.-Q. Sn/SnO$_x$ Core-Shell Nanospheres Synthesis, Anode Performance in Li Ion Batteries, and Superconductivity. *J. Phys. Chem. C* **2010**, *114*, 14697−14703.

(32) Hu, R.; Sun, W.; Liu, H.; Zeng, M.; Zhu, M. The Fast Filling of Nano-SnO$_2$ in CNTs by Vacuum Absorption: A New Approach to Realize Cyclic Durable Anodes for Lithium Ion Batteries. *Nanoscale* **2013**, *5*, 11971−11979.

(33) Mao, O.; Dunlap, R. A.; Dahn, J. R. Mechanically Alloyed Sn-Fe(-C) Powders as Anode Materials for Li-Ion Batteries - I. The Sn$_2$Fe-C System. *J. Electrochem. Soc.* **1999**, *146*, 405−413.

(34) Zou, Y. Q.; Wang, Y. Sn@CNT Nanostructures Rooted in Graphene with High and Fast Li-Storage Capacities. *ACS Nano* **2011**, *5*, 8108−8114.

(35) Mahmood, N.; Zhang, C. Z.; Liu, F.; Zhu, J. H.; Hou, Y. L. Hybrid of Co$_3$Sn$_2$@Co Nanoparticles and Nitrogen-Doped Graphene as a Lithium Ion Battery Anode. *ACS Nano* **2013**, *7*, 10307−10318.

(36) Wu, Z. S.; Ren, W. C.; Wen, L.; Gao, L. B.; Zhao, J. P.; Chen, Z. P.; Zhou, G. M.; Li, F.; Cheng, H. M. Graphene Anchored with Co$_3$O$_4$ Nanoparticles as Anode of Lithium Ion Batteries with Enhanced Reversible Capacity and Cyclic Performance. *ACS Nano* **2010**, *4*, 3187−3194.

(37) Lv, D.; Gordin, M. L.; Yi, R.; Xu, T.; Song, J.; Jiang, Y.-B.; Choi, D.; Wang, D. GeO$_x$/Reduced Graphene Oxide Composite as an Anode for Li-Ion Batteries: Enhanced Capacity via Reversible Utilization of Li$_2$O Along with Improved Rate Performance. *Adv. Funct. Mater.* **2014**, *24*, 1059−1066.

(38) Ji, L. W.; Tan, Z. K.; Kuykendall, T.; An, E. J.; Fu, Y. B.; Battaglia, V.; Zhang, Y. G. Multilayer Nanoassembly of Sn-Nanopillar Arrays Sandwiched between Graphene Layers for High-Capacity Lithium Storage. *Energy Environ. Sci.* **2011**, *4*, 3611−3616.

(39) Wang, G.; Shen, X.; Yao, J.; Park, J. Graphene Nanosheets for Enhanced Lithium Storage in Lithium Ion Batteries. *Carbon* **2009**, *47*, 2049−2053.

(40) Beaulieu, L. Y.; Beattie, S. D.; Hatchard, T. D.; Dahn, J. R. The Electrochemical Reaction of Lithium with Tin Studied by in Situ AFM. *J. Electrochem. Soc.* **2003**, *150*, A419−A424.

(41) Zhu, Y.; Wang, C. Galvanostatic Intermittent Titration Technique for Phase- Transformation Electrodes. *J. Phys. Chem. C* **2010**, *114*, 2830−2841.

(42) Lin, Y. M.; Klavetter, K. C.; Abel, P. R.; Davy, N. C.; Snider, J. L.; Heller, A.; Mullins, C. B. High Performance Silicon Nanoparticle Anode in Fluoroethylene Carbonate-Based Electrolyte for Li-Ion Batteries. *Chem. Commun.* **2012**, *48*, 7268−7270.